

Investigating spinning test particles: spin supplementary conditions and the Hamiltonian formalism

Georgios Lukes-Gerakopoulos,^{1,*} Jonathan Seyrich,^{2,†} and Daniela Kunst^{3,‡}

¹*Theoretical Physics Institute, University of Jena, 07743 Jena, Germany*

²*Mathematisches Institut, Universität Tübingen, Auf der Morgenstelle, 72076 Tübingen, Germany*

³*ZARM, University of Bremen, Am Fallturm, 28359 Bremen, Germany*

In this paper we report the results of a thorough numerical study of the motion of spinning particles in Kerr spacetime with different prescriptions. We first evaluate the Mathisson-Papapetrou equations with two different spin supplementary conditions, namely, the Tulczyjew and the Newton-Wigner, and make a comparison of these two cases. We then use the Hamiltonian formalism given by Barausse, Racine, and Buonanno in [*Phys. Rev. D* **80**, 104025 (2009)] to evolve the orbits and compare them with the corresponding orbits provided by the Mathisson-Papapetrou equations. We include a full description of how to treat the issues arising in the numerical implementation.

PACS numbers:

Keywords:

1. INTRODUCTION

Since we expect that the centers of galaxies are occupied by supermassive black holes, relativistic binary systems with extreme mass ratios are of great interest. A first approximation to an extreme mass ratio inspiral (EMRI) is the geodesic motion where the spin of the smaller particle is ignored. More relevant models have to incorporate the spin. This, however, appears not to be so simple.

The equations of motion of a spinning particle were given by Mathisson [1] and Papapetrou [2] several decades ago. The Mathisson-Papapetrou (MP) equations are not a closed set of first order ordinary differential equations, i.e., there are less equations than necessary in order to evolve the system. To close the set, an extra spin supplementary condition (SSC) is required. Over the years, various such SSCs have been proposed (see, e.g., [3, 4] for a review).

As a SSC fixes a center of reference, e.g., the center of the mass, and different SSCs define different centers, for each SSC we have a different world line (see, e.g., [4]), and, hence, each SSC prescribes a different evolution of the MP equations. But, although this ambiguity appears to be a major issue in the modeling of an EMRI binary system, the difference in the evolution caused by different SSCs has not received the adequate attention. Our work aims at quantifying those evolution differences in a Kerr spacetime background.

The first part of the study addresses the above issue by examining how “similar” initial conditions diverge when they are evolved by using different SSCs. We focus on two SSCs, namely the Tulczyjew (T) SSC [5] and the Newton-Wigner (NW) SSC [6], as introduced by Ba-

rausse et al. in [7]. T SSC is a standard SSC that has been used in several works concerned with different topics, see, e.g., [3, 4, 10–16]. On the other hand, NW SSC has been successfully implemented in the framework of the Post-Newtonian approximation [17, 18], and it is the only SSC allowing for a canonical Hamiltonian formalism, albeit only up to linear order in the spin of the particle in curved spacetimes. This Hamiltonian formalism has been derived in [7]. As it has many practical advantages to have a Hamiltonian formulation of a given problem at hand, for example because it is part of the effective one body formulation [7, 8], it would be nice to see if orbits obtained via the Hamiltonian formalism of [7] stay close to those obtained with the help of the full MP equations in the case of NW SSC (a discussion on the topic can be found in Sec. IV of [9]). Therefore, in the second part of our work, we compare both approaches numerically.

A numerical investigation of the equations considered in this work entails a bunch of interesting numerical challenges. To start with, a useful study of the divergence of different orbits should straddle a reasonably long time interval. The efficient integration of equations of motion over a long time interval requires structure preserving algorithms (see, e.g., [19] for an elaborate overview) such as symplectic schemes, which have been successfully applied for simulations in various fields of general relativity, e.g., [20–23]. Moreover, the MP equations have no Hamiltonian structure, wherefore one would expect usual symplectic integration schemes to lose their theoretical advantage over ordinary, not so efficient ones. What is more, in the NW SSC case part of the equations of motion will turn out to be known only implicitly. In this work we will explain how, notwithstanding the just mentioned obstacles, the MP equations can be evolved accurately in an efficient way for both SSCs. When comparing orbits calculated via the MP equations with those obtained by the Hamiltonian equations of [7], one is faced with the problem of different evolution parameters. We thus come up with a comfortable way of guaranteeing output at consistent times.

*Electronic address: gglukes@gmail.com

†Electronic address: seyrich@na.uni-tuebingen.de

‡Electronic address: daniela.kunst@zarm.uni-bremen.de

The paper is organized as follows. In Sec. 2 we introduce the MP equations and give a brief discussion on the SSCs. Then, we turn to the Hamiltonian formalism in Sec. 3, where the basic elements concerning the Hamiltonian function, which describes the motion of a spinning particle in curved spacetime, are summarized. In Sec. 4 we explain how the simulations with the MP equations are done, and a comparison between the T and the NW SSC is provided, whilst Sec. 5 quantifies the difference in the evolution of orbits between the MP equations and their Hamiltonian approximation. Finally, we discuss our main results in Sec. 6. A detailed discussion of the numerical implementation is provided in the Appendix (Secs. A and B).

The units we use are geometric ($G = c = 1$), and the signature of the metric is $(-, +, +, +)$. Greek letters denote the indices corresponding to spacetime (running from 0 to 3), while Latin ones denote indices corresponding only to space (running from 1 to 3). We use capital letters for the indices when referring to a flat spacetime. In general, we try to follow the notation in [7] whenever this is possible.

2. MATHISSON-PAPAPETROU EQUATIONS

The Mathisson-Papapetrou equations describe the motion of a particle with mass μ and spin $S^{\mu\nu}$ (pole-dipole approximation) in a given background $g_{\mu\nu}$. Their formulation in [10] reads

$$\frac{D p^\mu}{d\tau} = -\frac{1}{2} R^\mu{}_{\nu\kappa\lambda} v^\nu S^{\kappa\lambda} , \quad (1)$$

$$\frac{D S^{\mu\nu}}{d\tau} = p^\mu v^\nu - v^\mu p^\nu , \quad (2)$$

where p^μ is the four-momentum, $v^\mu = dx^\mu/d\tau$ is the tangent vector to the worldline along which the particle moves, τ is the proper time along this worldline, and $R^\mu{}_{\nu\kappa\lambda}$ is the Riemann tensor. In the case of a stationary and axisymmetric spacetime, the energy

$$E = -p_t + \frac{1}{2} g_{t\mu,\nu} S^{\mu\nu} , \quad (3)$$

and the z angular momentum

$$J_z = p_\phi - \frac{1}{2} g_{\phi\mu,\nu} S^{\mu\nu} , \quad (4)$$

are preserved along the solutions of the MP equations.

Since we selected τ to be the proper time, it holds that $v^\nu v_\nu = -1$. By multiplying Eq. (2) with v_ν we get

$$p^\mu = m v^\mu - v_\nu \frac{D S^{\mu\nu}}{d\tau} , \quad (5)$$

where $m = -p^\nu v_\nu$ is the rest mass of the particle with respect to v^ν , while the measure of the four-momentum $p^\nu p_\nu = -\mu^2$ provides the rest mass μ with respect to p^μ .

$m = \mu$ holds only if the tangent vector v^ν coincides with the four-velocity $u^\nu = p^\nu/\mu$.

It is useful to stress that neither of the masses have to be a constant of motion. Namely, for m we get

$$\frac{dm}{d\tau} = \frac{D m}{d\tau} = -\frac{D v_\nu}{d\tau} p^\nu ,$$

since from Eq. (1) we see that $\frac{D p^\nu}{d\tau} v_\nu = 0$, and by using Eq. (5) for replacing p^ν , we arrive at

$$\frac{dm}{d\tau} = \frac{D v_\nu}{d\tau} v_\mu \frac{D S^{\nu\mu}}{d\tau} . \quad (6)$$

For μ we have

$$\frac{d\mu}{d\tau} = \frac{D \mu}{d\tau} = -\frac{p_\nu}{\mu} \frac{D p^\nu}{d\tau} ,$$

and again by using Eq. (5) for replacing p^ν , we get

$$\frac{d\mu}{d\tau} = \frac{D p_\nu}{d\tau} \frac{p_\mu}{\mu m} \frac{D S^{\nu\mu}}{d\tau} . \quad (7)$$

The same holds for the spin measure

$$S^2 = \frac{1}{2} S_{\mu\nu} S^{\mu\nu} . \quad (8)$$

Here, we have

$$\frac{d S^2}{d\tau} = \frac{D S^2}{d\tau} = S_{\mu\nu} \frac{D S^{\mu\nu}}{d\tau} , \quad (9)$$

and by Eq. (2) we get

$$\begin{aligned} \frac{d S^2}{d\tau} &= S_{\mu\nu} (p^\mu v^\nu - v^\mu p^\nu) \\ &= 2 S_{\mu\nu} p^\mu v^\nu , \end{aligned} \quad (10)$$

which becomes zero if

$$S_{\mu\nu} p^\mu = 0 , \quad (11)$$

or

$$S_{\mu\nu} v^\mu = 0 . \quad (12)$$

Eq. (11) is the Tulczyjew SSC, while Eq. (12) is the Pirani SSC [24]. From Eq. (7) we see that $d\mu/d\tau = 0$ for T SSC, while for Pirani SSC $dm/d\tau = 0$. The MP equations with Pirani SSC exhibit a ‘‘strange’’ helical motion (see, e.g., [4]), which has been considered as unphysical. However, recently, in [25] the authors argued that the helical motion can be interpreted by the concept of a hidden electromagnetic-like momentum. We will not discuss Pirani SSC further. Instead, we are going to focus on the Newton-Wigner SSC, which reads

$$S^{\mu\nu} \omega_\mu = 0 , \quad (13)$$

where ω_μ is a time-like vector, or a sum of time-like vectors, e.g., of p_μ and φ_μ , i.e.,

$$\omega_\mu = p_\mu + \mu \varphi_\mu \quad . \quad (14)$$

In general, for NW SSC, neither the masses, Eqs. (6), (7), nor the spin, Eq. (2), are preserved. Thus, from this point of view it is a strange selection of a SSC. However, we should keep in mind that our framework is a pole-dipole approximation. Therefore it is somehow adequate for the just mentioned quantities to be conserved only up to linear order in the spin. For the spin, this can be seen from Eq. (9) but for the mass μ the proof is quite more complicated and was provided in [7].

2.1. Spin four-vector

Instead of the spin tensor $S^{\mu\nu}$, a spin four-vector S^μ is used sometimes, since S^μ is often considered more physically intuitive and more convenient than $S^{\mu\nu}$ (see, e.g., [26]).

For the T SSC the four-vector is defined by

$$S_\mu = -\frac{1}{2}\eta_{\mu\nu\rho\sigma}u^\nu S^{\rho\sigma} \quad , \quad (15)$$

where $\eta_{\mu\nu\rho\sigma}$ is the Levi-Civita density tensor

$$\eta_{\mu\nu\rho\sigma} = \sqrt{-g} \epsilon_{\mu\nu\rho\sigma} \quad , \quad (16)$$

and $\epsilon_{\mu\nu\rho\sigma}$ is the Levi-Civita symbol with $\epsilon_{0123} = -1$. The inverse relation of Eq. (15) between the two spin forms is

$$S^{\rho\sigma} = -\eta^{\rho\sigma\gamma\delta} S_\gamma u_\delta \quad . \quad (17)$$

By replacing the last equation in Eq. (8), we get

$$S^2 = S_\mu S^\mu \quad . \quad (18)$$

From Eq. (15) we see that

$$S_\mu p^\mu = 0 \quad , \quad (19)$$

so the spin four vector is perpendicular to the momentum.

For the NW SSC we define the four-vector as

$$S_\mu = -\frac{1}{2\mu}\eta_{\mu\nu\rho\sigma}\omega^\nu S^{\rho\sigma} \quad . \quad (20)$$

By this definition we fix that

$$S_\mu \omega^\mu = 0 \quad . \quad (21)$$

Thus, the spin four vector is perpendicular to the time-like vector ω_μ . In the NW case the inverse relation of Eq. (20) between the two spin forms is

$$S^{\rho\sigma} = \eta^{\rho\sigma\gamma\delta} S_\gamma \frac{\mu \omega_\delta}{\omega_\nu \omega^\nu} \quad . \quad (22)$$

Now, the spin measure (8) reads

$$S^2 = -\frac{\mu^2}{\omega_\nu \omega^\nu} S_\sigma S^\sigma \quad . \quad (23)$$

The measure of the spin divided by the rest mass, i.e., S/μ defines the minimal radius of a volume which a spinning body has to have in order not to rotate with superluminal speed. The same radius defines the upper bound of the separation between worldlines defined by various SSCs, i.e., a disc of centers of mass inside of which the worldlines have to lie. This radius was introduced by Möller in [27] and, therefore, is often referred to as the Möller radius.

In the next step, we explain how to calculate the tangent vector v^μ .

2.2. Calculating the tangent vector

The MP equations do not explicitly state how we can evaluate the tangent vector v^μ throughout the evolution. To find v^μ we use the SSCs.

In the case of T SSC, v^μ is found via the relation

$$v^\mu = N(u^\mu + w^\mu) \quad , \quad (24)$$

where

$$w^\mu = \frac{2 S^{\mu\nu} u^\lambda R_{\nu\lambda\rho\sigma} S^{\rho\sigma}}{4 \mu^2 + R_{\alpha\beta\gamma\delta} S^{\alpha\beta} S^{\gamma\delta}} \quad , \quad (25)$$

and, because $v^\mu v_\mu = -1$, we get

$$N = \frac{1}{\sqrt{1 - w_\mu w^\mu}} \quad . \quad (26)$$

For more details on how to derive the above expression see, e.g., [3].

In the case of NW SSC, according to our knowledge, there is no explicit expression which gives v^μ as a function of p^μ and $S^{\mu\nu}$. However, by taking the covariant derivative of Eq. (13), we obtain

$$v^\mu = \frac{1}{\omega_\nu p^\nu} \left((\omega_\nu v^\nu) p^\mu + S^{\mu\nu} \frac{D \omega_\nu}{d\tau} \right) \quad . \quad (27)$$

A detailed discussion on how we solve the initial value problem numerically is provided in Appendix A.

3. THE HAMILTONIAN FORMALISM FOR THE SPINNING PARTICLE

The MP equations (1), (2) can be derived by means of Lagrangian mechanics, see, e.g., [28–30]. If we want to apply a Legendre transformation in order to get a Hamiltonian canonical formulation [35] for a spinning particle moving in a curved spacetime, then the canonical structure holds only at linear order of the particle's spin [7].

The spin in the Hamiltonian formalism proposed by [7] comes from the projection of the spin tensor $S^{\mu\nu}$ onto the spacelike part of a tetrad field \tilde{e}_Δ^μ . This tetrad consists of a timelike future oriented vector \tilde{e}_T^μ (throughout the article we shall use T instead of 0) and three spacelike vectors \tilde{e}_I^μ . For the tetrad it holds that

$$\tilde{e}_\Gamma^\mu \tilde{e}_\Delta^\nu g_{\mu\nu} = \eta_{\Gamma\Delta} \quad , \quad (28)$$

where $\eta_{\Gamma\Delta}$ is the metric of the flat spacetime, and

$$\tilde{e}_\Delta^\mu \tilde{e}_\nu^\Delta = \delta_\nu^\mu \quad , \quad (29)$$

where δ_ν^μ is the Kronecker delta. The capital indices are raised or lowered by the flat metric. When a tensor is denoted with capital indices, then the tensor has been projected onto this tetrad \tilde{e}_Δ^μ . In the case of the spin tensor $S^{\mu\nu}$, the projection reads

$$S^{IJ} = S^{\mu\nu} \tilde{e}_\mu^I \tilde{e}_\nu^J \quad . \quad (30)$$

The remaining components of this projection come from splitting the NW SSC (13) appropriately, and projecting the split on the tetrad, i.e.,

$$S^{TI} = S^{IJ} \frac{\omega_J}{\omega_T} \quad , \quad (31)$$

where $\omega_\Delta = \tilde{e}_\Delta^\nu \omega_\nu$ is the projection of the time-like vector (14) of the NW SSC (13) as chosen in [7]

$$\omega_\nu = p_\nu - \mu \tilde{e}_\nu^T \quad (32)$$

on the tetrad field, i.e.,

$$\begin{aligned} \omega_T &= p_\nu \tilde{e}_T^\nu - \mu \quad , \\ \omega_J &= p_\nu \tilde{e}_J^\nu \quad . \end{aligned} \quad (33)$$

However, the Hamiltonian function of the spinning particle given in [7] does not use exactly the above described spin projection, instead the spin three vector is employed, i.e.,

$$S_I = \frac{1}{2} \epsilon_{IJJ} S^{JL} \quad (34)$$

(the inversion of Eq. (34) gives $S^{JL} = -\epsilon^{JLI} S_I$).

The Hamiltonian function H itself

$$H = H_{NS} + H^C S_C \quad , \quad (35)$$

splits in two parts. The first

$$H_{NS} = \beta^i P_i + \alpha \sqrt{\mu^2 + \gamma^{ij} P_i P_j} \quad (36)$$

is the Hamiltonian for a non-spinning particle, and the second $H^C S_C$

$$H^C = - \left(\beta^i F_i^C + F_0^C + \frac{\alpha \gamma^{ij} P_i F_j^C}{\sqrt{\mu^2 + \gamma^{ij} P_i P_j}} \right) \quad (37)$$

includes the elements describing the spin, where

$$\alpha = \frac{1}{\sqrt{-g^{00}}} \quad , \quad (38)$$

$$\beta^i = \frac{g^{0i}}{g^{00}} \quad , \quad (39)$$

$$\gamma^{ij} = g^{ij} - \frac{g^{0i} g^{0j}}{g^{00}} \quad . \quad (40)$$

The canonical momenta P_i conjugate to x^i of the Hamiltonian (35) can be calculated from the momenta p_i of the MP formulation by using the relation

$$\begin{aligned} P_i &= p_i + E_{i\Gamma\Delta} S^{\Gamma\Delta} \quad , \\ &= p_i + \left(2E_{iTJ} \frac{\omega_C}{\omega_T} + E_{iJC} \right) \epsilon^{JCL} S_L \quad , \end{aligned} \quad (41)$$

where

$$E_{\nu\Gamma\Delta} = -\frac{1}{2} \left(g_{\kappa\lambda} \tilde{e}_\Gamma^\kappa \frac{\partial \tilde{e}_\Delta^\lambda}{\partial x^\nu} + \tilde{e}_\Gamma^\kappa \Gamma_{\kappa\nu\lambda} \tilde{e}_\Delta^\lambda \right) \quad (42)$$

is a tensor which is antisymmetric in the last two indices, i.e., $E_{\nu\Gamma\Delta} = -E_{\nu\Delta\Gamma}$. $\Gamma_{\kappa\nu\lambda}$, in turn, are the Christoffel symbols. This choice of momenta leads to a set of phase space variables that are canonical at linear order in the particle's spin.

Finally, the F_μ^C tensor in Eq. (35) reads

$$F_\mu^C = \left(2E_{\mu TI} \frac{\bar{\omega}_J}{\bar{\omega}_T} + E_{\mu IJ} \right) \epsilon^{IJC} \quad , \quad (43)$$

where

$$\begin{aligned} \bar{\omega}_\Delta &= \bar{\omega}_\nu \tilde{e}_\Delta^\nu \quad , \\ \bar{\omega}_\nu &= \bar{P}_\nu - \mu \tilde{e}_\nu^T \quad , \\ \bar{P}_i &= P_i \quad , \\ \bar{P}_0 &= -\beta^i P_i - \alpha \sqrt{\mu^2 + \gamma^{ij} P_i P_j} \quad , \\ \bar{\omega}_T &= \bar{P}_\nu \tilde{e}_T^\nu - \mu \quad , \\ \bar{\omega}_J &= \bar{P}_\nu \tilde{e}_J^\nu \quad . \end{aligned} \quad (44)$$

The equations of motion for the canonical variables as a function of coordinate time t , as derived in [7], read

$$\frac{dx^i}{dt} = \frac{\partial H}{\partial P_i} \quad , \quad (45)$$

$$\frac{dP_i}{dt} = -\frac{\partial H}{\partial x^i} \quad , \quad (46)$$

$$\frac{dS_I}{dt} = \epsilon_{IJC} \frac{\partial H}{\partial S_J} S^C \quad . \quad (47)$$

The formulation provided up to this point is general, namely it does not depend on the coordinate or on the tetrad field choice. In the next section we specify the setup we use in the numerical sections of our work.

3.1. The Hamiltonian for the Kerr spacetime

The line element of the Kerr spacetime in Boyer-Lindquist coordinates is

$$ds^2 = g_{tt} dt^2 + 2 g_{t\phi} dt d\phi + g_{\phi\phi} d\phi^2 + g_{rr} dr^2 + g_{\theta\theta} d\theta^2 , \quad (48)$$

where

$$\begin{aligned} g_{tt} &= -1 + \frac{2Mr}{\Sigma} , \\ g_{t\phi} &= -\frac{2aMr \sin^2 \theta}{\Sigma} , \\ g_{\phi\phi} &= \frac{\Lambda \sin^2 \theta}{\Sigma} , \\ g_{rr} &= \frac{\Sigma}{\Delta} , \\ g_{\theta\theta} &= \Sigma , \end{aligned} \quad (49)$$

and

$$\begin{aligned} \Sigma &= r^2 + a^2 \cos^2 \theta , \\ \Delta &= \varpi^2 - 2Mr , \\ \varpi^2 &= r^2 + a^2 , \\ \Lambda &= \varpi^4 - a^2 \Delta \sin^2 \theta . \end{aligned} \quad (50)$$

In this section we reproduce the quantities already presented in [7]. In the case of the small indices, we replace

the numbers with the coordinates , i.e., t, r, θ, ϕ stand for 0, 1, 2, 3, respectively. The capital indices, meanwhile, are left unaltered. M denotes the mass and a the spin parameter of the central Kerr black hole.

The tetrad we use has been provided in [7] and reads

$$\begin{aligned} \tilde{e}_\mu^T &= \delta_\mu^t \sqrt{\frac{\Delta \Sigma}{\Lambda}} , \\ \tilde{e}_\mu^1 &= \delta_\mu^r \sqrt{\frac{\Sigma}{\Delta}} , \\ \tilde{e}_\mu^2 &= \delta_\mu^\theta \sqrt{\Sigma} , \\ \tilde{e}_\mu^3 &= -\delta_\mu^t \frac{2aMr \sin \theta}{\sqrt{\Lambda \Sigma}} + \delta_\mu^\phi \sin \theta \sqrt{\frac{\Lambda}{\Sigma}} , \end{aligned} \quad (51)$$

while the inverse one reads

$$\begin{aligned} \tilde{e}_T^\mu &= \delta_t^\mu \sqrt{\frac{\Lambda}{\Delta \Sigma}} + \delta_\phi^\mu \frac{2aMr}{\sqrt{\Delta \Lambda \Sigma}} , \\ \tilde{e}_1^\mu &= \delta_r^\mu \sqrt{\frac{\Delta}{\Sigma}} , \\ \tilde{e}_2^\mu &= \delta_\theta^\mu \frac{1}{\sqrt{\Sigma}} , \\ \tilde{e}_3^\mu &= \delta_\phi^\mu \frac{1}{\sin \theta} \sqrt{\frac{\Sigma}{\Lambda}} . \end{aligned} \quad (52)$$

By calculating all the quantities mentioned in Sec. 3, we finally obtain the coefficients H^C (Eq. (37)) as

$$\begin{aligned} H^1 &= -\frac{\sqrt{\Delta} \cos \theta}{\sqrt{Q}(1+\sqrt{Q})\Lambda^2\sqrt{\Sigma} \sin^2 \theta} [(1+\sqrt{Q})(\Delta \Sigma^2 + 2Mr\varpi^4) + \sqrt{Q}2a^2Mr\varpi^2 \sin^2 \theta] \frac{P_\phi}{\mu} \\ &+ \frac{aM(2r^2\Sigma + \varpi^2\rho^2) \sin \theta \Delta P_r P_\theta}{\sqrt{Q}(1+\sqrt{Q})\Lambda^{3/2}\Sigma^2} + \frac{2a^3Mr \cos \theta \sin^2 \theta \Delta}{\sqrt{Q}(1+\sqrt{Q})\Lambda^{3/2}\Sigma} \left(1 + \sqrt{Q} + \frac{2\Sigma}{\Lambda \sin^2 \theta} \frac{P_\phi^2}{\mu^2} + \frac{\Delta}{\Sigma} \frac{P_r^2}{\mu^2} \right) , \\ H^2 &= \frac{\Delta(1+\sqrt{Q})(r\Sigma^2 - a^2M\rho^2 \sin^2 \theta) - M\sqrt{Q}(\rho^2\varpi^4 - 4a^2Mr^3 \sin^2 \theta)}{\sqrt{Q}(1+\sqrt{Q})\Lambda^2\sqrt{\Sigma} \sin \theta} \frac{P_\phi}{\mu} + \frac{2a^3Mr \cos \theta \sin^2 \theta \Delta^{3/2} P_r P_\theta}{\sqrt{Q}(1+\sqrt{Q})\Lambda^{3/2}\Sigma^2} \frac{P_\theta}{\mu^2} \\ &+ \frac{aM(2r^2\Sigma + \varpi^2\rho^2) \sin \theta \sqrt{\Delta}}{\sqrt{Q}(1+\sqrt{Q})\Lambda^{3/2}\Sigma} \left(1 + \sqrt{Q} + \frac{2\Sigma}{\Lambda \sin^2 \theta} \frac{P_\phi^2}{\mu^2} + \frac{1}{\Sigma} \frac{P_\theta^2}{\mu^2} \right) , \\ H^3 &= -\frac{a^2\Delta \cos \theta \sin \theta}{\sqrt{Q}(1+\sqrt{Q})(\Lambda\Sigma)^{3/2}} (\Lambda + \sqrt{Q}\Delta\Sigma) \frac{P_r}{\mu} - \frac{r\Lambda\Delta + \varpi^2\Sigma\sqrt{Q}(r\Delta - M(r^2 - a^2))}{\sqrt{Q}(1+\sqrt{Q})(\Lambda\Sigma)^{3/2}} \frac{P_\theta}{\mu} \\ &- \frac{aM\sqrt{\Delta}}{\mu^2\sqrt{Q}(1+\sqrt{Q})\Lambda^2\Sigma} [2a^2r\Delta \sin \theta \cos \theta P_r + (2r^2\Sigma + \varpi^2\rho^2)P_\theta] P_\phi , \end{aligned} \quad (53)$$

where

$$\begin{aligned} Q &= 1 + \frac{\gamma^{ij}}{\mu^2} P_i P_j \\ &= 1 + \mu^{-2} \left(\frac{\Delta}{\Sigma} P_r^2 + \frac{1}{\Sigma} P_\theta^2 + \frac{\Sigma}{\Lambda \sin^2 \theta} P_\phi^2 \right) , \end{aligned} \quad (54)$$

and

$$\rho^2 = r^2 - a^2 \cos^2 \theta . \quad (55)$$

For a full and detailed presentation of the derivation of H^C , we refer the reader to [7].

It is worth mentioning here that, contrary to the T SSC, the NW SSC (Eq. (32)) does not uniquely define the reference worldline. As already noted in the introduction the choice of the center of mass, i.e., the reference worldline, is observer dependent. When T SSC is applied the zero 3-momentum observer is chosen. However, when the NW SSC is used there is no unique choice because the observer and therewith the reference worldline depends on the tetrad. We have fixed our tetrad in Eqs. (51), (52). In the following we only consider the evolution of the orbit corresponding to this observer so that we do not have to worry about transforming the dynamical properties of the system to another reference frame.

4. COMPARISON OF TULCZYJEW AND NEWTON-WIGNER SSC

4.1. Preliminaries

When simulating the MP equations we in fact have to solve the initial value problem

$$\left\{ \begin{array}{l} \frac{d x^\mu}{d\tau} = v^\mu, \\ \frac{d p^\mu}{d\tau} = -\frac{1}{2} R^\mu{}_{\nu\kappa\lambda} v^\nu S^{\kappa\lambda} - \Gamma^\mu{}_{\nu\kappa} v^\nu p^\kappa, \\ \frac{d S^{\mu\nu}}{d\tau} = p^\mu v^\nu - v^\mu p^\nu + \Gamma^\mu{}_{\kappa\lambda} S^{\nu\kappa} v^\lambda - \Gamma^\nu{}_{\kappa\lambda} S^{\mu\kappa} v^\lambda, \\ x^\mu(\tau = 0) = x_0^\mu, \\ p^\mu(\tau = 0) = p_0^\mu, \\ S^{\mu\nu}(\tau = 0) = S_0^{\mu\nu}. \end{array} \right. \quad (56)$$

As a first step, we have to provide initial conditions which comply with the constraints mentioned earlier (Sec. 2).

In order to find these appropriate initial conditions, we follow the approach given in [13], which implies that instead of the spin tensor $S^{\mu\nu}$ we use the vector S^μ for the initial setup. Without loss of generality, we set $t = \phi = 0$ and provide initial values for r , θ , p^r as well as for the two spin components S^r and S^θ . The other initial conditions, namely p^t , p^θ , p^ϕ , S^t , and S^ϕ , are then fixed by the constraints. In the case of the T SSC, those constraints are

$$E = -p_t - \frac{1}{2\mu} g_{t\mu,\nu} \eta^{\mu\nu\gamma\delta} S_\gamma p_\delta, \quad (57)$$

$$J_z = p_\phi + \frac{1}{2\mu} g_{\phi\mu,\nu} \eta^{\mu\nu\gamma\delta} S_\gamma p_\delta, \quad (58)$$

$$\mu^2 = -g^{\mu\nu} p_\mu p_\nu, \quad (59)$$

$$S^2 = g^{\mu\nu} S_\mu S_\nu, \quad (60)$$

$$0 = g^{\mu\nu} S_\mu p_\nu, \quad (61)$$

where we have substituted Eq. (17) into the constants of motion (3), (4), and lowered the indices wherever needed. Thus, we specify an orbit by providing values for E , J_z , S^2 , and μ^2 . We then solve the system (57)-(61) for p_t , p_θ , p_ϕ , S_t , and S_ϕ with the help of the Newton-Raphson method.

For comparing the effect of different SSCs in the evolution of MP, we need to find initial conditions for the NW SSC which are similar to the T SSC case. Hence, we parametrize the orbits by providing the same initial set of values for r , θ , p^r , S^r , S^θ , E , J_z , S^2 and μ^2 . The set of constraints for the NW SSC is similar to the one for the T SSC (Eqs. (57)-(61)). The constraints (57)-(58) remain unaltered. We use Eq. (59), and Eq. (23) instead of Eq. (60) for the initial setup, even though, in the case of the NW SSC, neither the spin S^2 nor the rest mass μ is preserved anymore. Finally, we replace constraint (61) by

$$g^{\mu\nu} S_\mu \omega_\nu = 0.$$

When solving the resulting system for p_t , p_θ , p_ϕ , S_t , and S_ϕ for the same provided r , θ , p^r , S^r , S^θ , E , J_z , S^2 and μ^2 as in the T case, we get what we referred to as similar initial conditions above. At last, by raising indices of the momenta and going from spin vectors to tensors with the help of the transformations (17) and (22), respectively, we get suitable data to start the computation with. The orbits are evolved through the Eqs. (1), (2). A more detailed discussion about the techniques we have applied to evolve the MP equations is provided in Appendix A.

The timelike vector ω_ν in the NW SSC (13) is given by Eq. (32), where the \tilde{e}_ν^T is the top equation from the set (51). By adapting the convention that times and lengths are measured in terms of M , we set $M = 1$ throughout the paper.

Before we proceed with the numerical results, we want to discuss the initial setup for our evaluations in this section. We have chosen the orbits to start from the same point in the configuration space, i.e., both worldlines at $\tau = 0$ lie at the same spacetime point. This means that both of the different corresponding observers see the center of the mass lying at the same place, even if the SSCs are different. This is not the usual way this subject is treated. In [4], for example, the discussion about the transition between two different SSCs is based on the center of the mass worldline displacement. The latter approach would not be appropriate for our treatment, because apart from the shift in the value of the spin tensor, the initial point in the configuration space should be shifted as well [4]. In our treatment we want to change the order of magnitude of the spin while keeping the initial conditions as similar as possible during the scaling, in order to observe how the two different SSCs converge as the geodesic limit is approached. In other words we do not attempt to have initial conditions which would obey the transition between different SSCs for one particle, but rather conditions which represent similar orbits for two different SSCs.

4.2. Comparison for large spin

In our first example, the parameters read $a = 0.5$, $r = 11.7$, $\theta = \pi/2$, $p^r = 0.1$, $S = 1$, $S^r = 0.1 S$, $S^\theta = 0.01 S$,

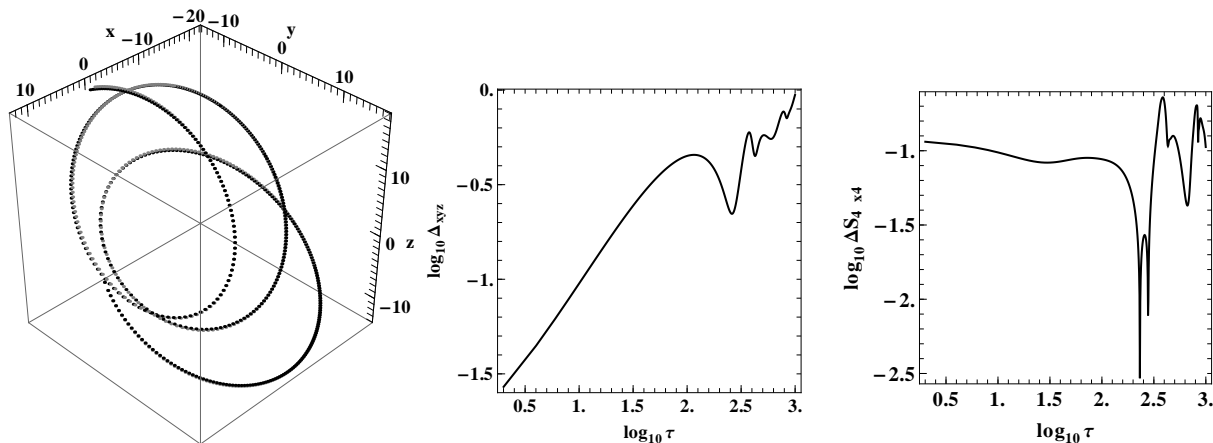


FIG. 1: The left panel shows a MP orbit with T SSC (black dots) and a MP orbit with NW SSC (gray dots) in the configuration space x , y , z (Cartesian coordinates). The common parameters for these orbits are $a = 0.5$, $r = 11.7$, $\theta = \pi/2$, $p^r = 0.1$, $S = 1$, $S^r = 0.1 S$, $S^\theta = 0.01 S$, $E = 0.97$, $J_z = 3$, and $\mu = 1$. The central panel shows the logarithm of the Euclidean distance in the configuration space between these two orbits as a function of the proper time. The right panel shows the logarithm of the difference $\Delta S_{4 \times 4}$ between the spin tensors of these two orbits as a function of the proper time.

$E = 0.97$, $J_z = 3$, and $\mu = 1$. The left panel of Fig. 1 shows how the two MP orbits with T SSC (black) and NW SSC (gray) evolve in the configuration space where the Cartesian coordinates

$$\begin{aligned} x &= r \cos \phi \sin \theta \quad , \\ y &= r \sin \phi \sin \theta \quad , \\ z &= r \cos \theta \quad , \end{aligned} \quad (62)$$

are employed.

The divergence between the two orbits is barely visible in the left panel, but if we take the Euclidean norm

$$\Delta_{xyz} = \sqrt{(x_T - x_{NW})^2 + (y_T - y_{NW})^2 + (z_T - z_{NW})^2} \quad , \quad (63)$$

we see that at the end of our run, the separation between the two orbits is of the order one (central panel of Fig. 1), while the radial distance from the central black hole is of the order ten (left panel of Fig. 1). Even if the Möller radius is not an appropriate tool for our setup (see the discussion at the last paragraph of Sec. 4.1), it is worthy to note that the two orbits lie inside a Möller radius ($S/\mu = 1$) for $\tau = 10^3$, even if their distance will grow out of this radius later on. This divergence in the orbit evolution follows the discrepancy in the spin space. To illustrate this, the norm of the difference between the spin tensor $S_T^{\mu\nu}$ of the T SSC and the spin tensor $S_T^{\mu\nu}$ of the NW SSC,

$$\Delta S_{4 \times 4} = \sqrt{|g_{\mu\nu} g_{\kappa\lambda} (S_T^{\nu\kappa} - S_{NW}^{\nu\kappa})(S_T^{\mu\lambda} - S_{NW}^{\mu\lambda})|} \quad , \quad (64)$$

is displayed in the right panel of Fig. 1. $\Delta S_{4 \times 4}$ is one tenth of the spin measure right from the beginning, and stays at this level during the evolution. Thus, from an orbital dynamic point of view when the spin of the test particle is of order $S = 1$, the choice of different SSCs leads to orbital evolutions which diverge significantly with time.

One thing that has to be discussed before we proceed is the meaning of a 'common' proper time, when two orbits with different SSCs are compared. Each SSC defines its own center of reference, which implies that with each SSC the proper time that is measured along the above orbits is different, even if the orbits start with similar initial conditions. Another issue that arises here is how we can measure the distance between two 'nearby' orbits in a curved spacetime. Above, we use the Euclidean norm, however the spacetime is not Euclidean. The same issues arise when geodesic chaos is studied in curved spacetimes (see, e.g., [31]). One of the suggestions in the aforementioned field is to use the two nearby orbits technique, i.e., to evolve two orbits with similar initial conditions and measure their distance when they reach the same proper time. This is in few words the approach we adapt in our study for the time issue. For the issue of the distance in the configuration space between the two orbits, we have chosen to employ the Euclidean metric. We could employ the local $g_{\mu\nu}$ metric as well, even if the orbits depart from each other significantly (middle panel of Fig. 5). However, for the evolution times $\tau = 10^3$ the results coming from both approaches are almost identical, and therefore we went for the the simplest metric, which is the Euclidean.

4.3. Comparison for very small spin

Since we mentioned the geodesic orbits, we approach this limit by setting the measure of the spin in our initial conditions to $S = 10^{-8}$. All the other parameters are the same as in Fig. 1. For this geodesic-like setup the orbits in the configuration space resemble the orbits shown in the left panel of Fig. 1. However, the left panel of Fig. 2 shows that the distance between the two orbits

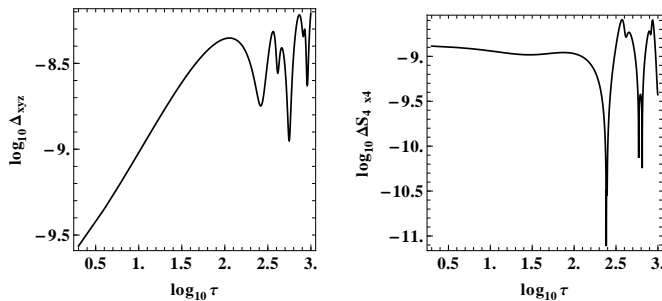


FIG. 2: The left panel shows the logarithm of the Euclidean distance in the configuration space between a MP orbit with T SSC and a MP orbit with NW SSC as a function of the proper time. The common parameters for these orbits read $a = 0.5$, $r = 11.7$, $\theta = \pi/2$, $p^r = 0.1$, $S = 10^{-8}$, $S^r = 0.1 S$, $S^\theta = 0.01 S$, $E = 0.97$, $J_z = 3$, and $\mu = 1$. The right panel shows the logarithm of the difference $\Delta S_{4 \times 4}$ between the spin tensors of these two orbits as a function of the proper time.

has dropped significantly, about 8 orders of magnitude. This drop is anticipated since we tend to the geodesic limit and the spin contribution is expected to be smaller. However, the level of the divergence in the configuration space (left panel of Fig. 2) is again defined by the magnitude of the spin difference $\Delta S_{4 \times 4}$ (right panel of Fig. 2). Namely, even though the initial conditions in the configuration space are identical, i.e., $\Delta_{xyz} = 0$, those of the spin components are not, i.e., $\Delta S_{4 \times 4} \approx 10^{-9}$, and this initial divergence in the spin space is passed on to the configuration space.

4.4. Constants of motion

We now turn our attention to the conservation of the four-momentum (rest mass μ) and of the spin S . In order to check whether these quantities are preserved, we use the relative error of the four-momentum

$$\Delta\mu^2 = \left| 1 - \frac{\mu^2(\tau)}{\mu^2(0)} \right|, \quad (65)$$

and the relative error of the spin S^2

$$\Delta S^2 = \left| 1 - \frac{S^2(\tau)}{S^2(0)} \right|, \quad (66)$$

where $\mu^2(\tau)$, and $S^2(\tau)$ are calculated at time τ .

We see from Fig. 3 that both the rest mass μ^2 and the spin are conserved for the T SSC (black lines) as was expected (see Sec. 2). On the other hand, in the case of the NW SSC (gray lines) the four-momentum scales with the magnitude of the spin S , while the square of the spin itself stays at the same level indifferently from the spin's magnitude. This scaling in the conservation of the mass is anticipated because, as $S \rightarrow 0$, the evolution of the MP equations approaches that of the geodesic motion.

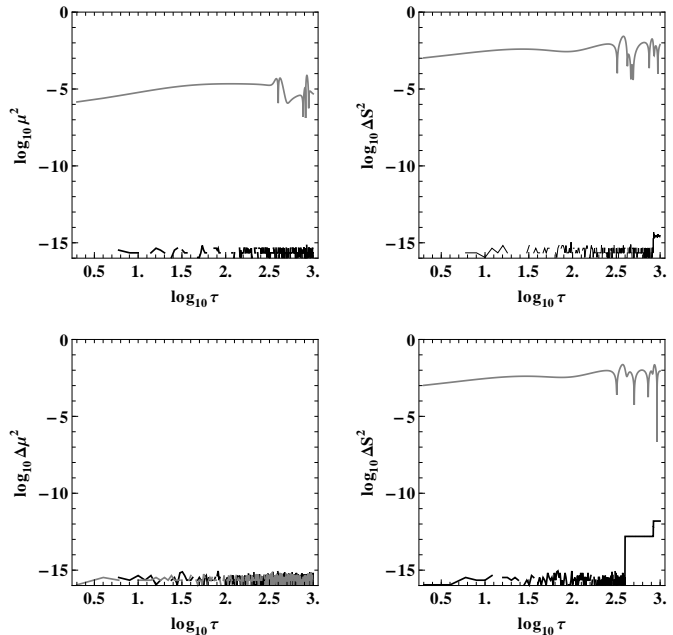


FIG. 3: The top row of panels corresponds to the orbits of Fig. 1, while the bottom row of panels corresponds to the orbits of Fig. 2. The black lines represent the evolution of the MP equations with T SSC, while the gray lines represent the NW SSC. The left column of panels shows the relative error in the preservation of the four-momentum, while the right depicts the preservation of the spin.

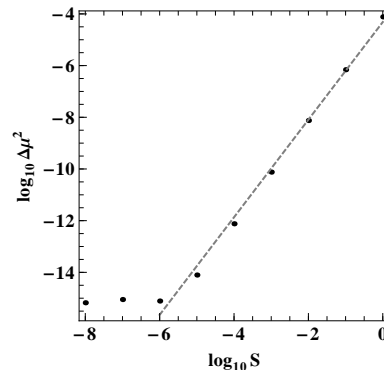


FIG. 4: The relative error of the four-momentum $\Delta\mu^2$ as a function of the spin measure S for the NW SSC. The black dots correspond to the maximum values of $\Delta\mu^2$ during the evolution for each S . The dashed line is a linear fit of the form $\log_{10} \Delta\mu^2 = a \log_{10} S + b$ for data with $S > 10^{-6}$, where $a = 1.995 \pm 0.004$, $b = -4.136 \pm 0.013$.

In order to better illustrate the above mentioned scaling, we run several simulations with initial setups similar to the one of Fig. 1 where we only change the measure of the spin, S . For every simulation, we plot the maximum value of $\Delta\mu^2$ along the trajectory against the initial spin measure (Fig. 4). The resulting plot shows that, as we decrease S , the four-momentum for the NW SSC tends

to be conserved up to the computational accuracy. There are two effects that shape this figure. One is the theoretical scaling of $\Delta\mu^2$ as a function of S and the other is the finite computational accuracy. From a linear fit of our data we get for $S > 10^{-6}$ (dashed line in Fig. 4) $\Delta\mu^2 \propto S^2$. For smaller spins a plateau appears because we reach the computational accuracy (in our runs we use double precision).

Since for T SSC the four-momentum is conserved and for the NW SSC the $\sqrt{\Delta\mu^2}$ scales linearly with the spin, this scaling can be interpreted as the rate by which the two different SSCs converge to each other. Changing the value of the spin a of the central black hole does not alter qualitatively the results of our numerical comparison.

5. NUMERICAL COMPARISON OF THE MP EQUATIONS WITH THE CORRESPONDING HAMILTONIAN EQUATIONS

5.1. Preliminaries

Since the MP equations are a pole-dipole approximation, multipoles of higher order than the spin dipole are already neglected. However, we can simplify the problem further by assuming that the physically relevant values for the particle spin are small and the terms quadratic in the spin correspond to the quadrupole contribution. Thus, a Hamiltonian which is accurate up to linear order of the spin should yield satisfactory results. This is the main idea on which the construction of such a Hamiltonian formalism for NW SSC in [7] was based.

According to this formalism (see the brief description in Sec. 3), the evolution parameter is not the proper time like in the case of Sec. 4, but the coordinate time. In order to perform a comparison between the MP equations and the corresponding Hamiltonian (Sec. 3.1) equations, we could rewrite our MP code with respect to the coordinate time. However, the coordinate times, at which our quantities were calculated in the MP simulations, were given as output anyway. With them at hand, there is an easier way out. One can evolve the Hamilton's equations of motion using constant steps in the coordinate time, and interpolate the solution around the required times of output. A more detailed discussion on this topic and the numerical methods we have used is given in Appendix B.

Moreover, in order to make the two formalisms comparable, we used the equations given in Sec. 3 to go from the set of variables $\{x^\mu, p^\mu, S^{\mu\nu}\}$ of the MP equations to the set of variables $\{x^i, P^i, S^I\}$ in the Hamiltonian formalism. Note that this holds also for the initial conditions, thus both the MP equations and the corresponding Hamilton's equations start with exactly the same initial setup.

Before showing the results of comparisons between the two approaches, we want to point out that all simulations using the Hamiltonian equations were much faster than their equivalents based on the MP equations with

NW SSC. More detailed information on this can be found in the Appendix Sections.

5.2. Comparison for large spin

Using the initial conditions for the NW SSC given in Fig. 1, we have evolved the orbit by using Hamilton's equations. The motion of the corresponding orbit in the configuration space is shown in the left panel of Fig. 5 (black dots) together with the orbit evolved through the MP equations (gray dots). Even if the two orbits start with the same initial conditions they depart from each other quite quickly. This is seen more clearly in the central panel of Fig. 5, where the Euclidean distance between the two orbits

$$\Delta_{xyz} = \sqrt{(x_H - x_{MP})^2 + (y_H - y_{MP})^2 + (z_H - z_{MP})^2}, \quad (67)$$

is displayed as a function of the coordinate time. Near the end of the calculation, the distance Δ_{xyz} is almost as large as the radial distance of the particle from the central black hole. From the appearance of the left panel of Fig. 5 one might wonder whether the divergence between the orbits is a ‘‘synchronization’’ issue. However, since both schemes use the same SSC, i.e., the NW SSC, and since the initial conditions for both schemes are exactly the same, i.e., the orbits correspond to the same particle, the proper time for both orbits has to tick at the same rate. Thus, it is reasonable to claim that this divergence results from the fact that the Hamiltonian is valid up to the linear order in the particle spin, and since the spin here is large, i.e., $S = 1$, such divergence should be expected. Nevertheless, it is impressive that orbits corresponding to the same particle evaluated with different schemes, i.e., the MP equations and the corresponding Hamiltonian, give a divergence that is of one order of magnitude larger than the divergence of the MP equations with different SSCs (left panel of Fig. 1). If we took the Möller radius as a criterion, for example, then, since the distance between the two orbits exceeds the diameter of the disc of centers of mass, according to this criterion, the orbits could not correspond to the same particle. Therefore, we can say that the Hamiltonian formalism is not valid for large spin values, just as expected.

The spin in the Hamiltonian formalism is given by the projection vector (Eq. (34)). The Euclidean norm of the difference between the spin vector S_H^I calculated by Hamilton's equations and the S_{MP}^I calculated by the MP equations

$$\Delta S_v = \sqrt{\sum_{I=1}^3 (S_H^I - S_{MP}^I)^2}, \quad (68)$$

is plotted as a function of the coordinate time in the right panel of Fig. 5. This plot shows that the difference is quite high, even if the spin values are identical at first.

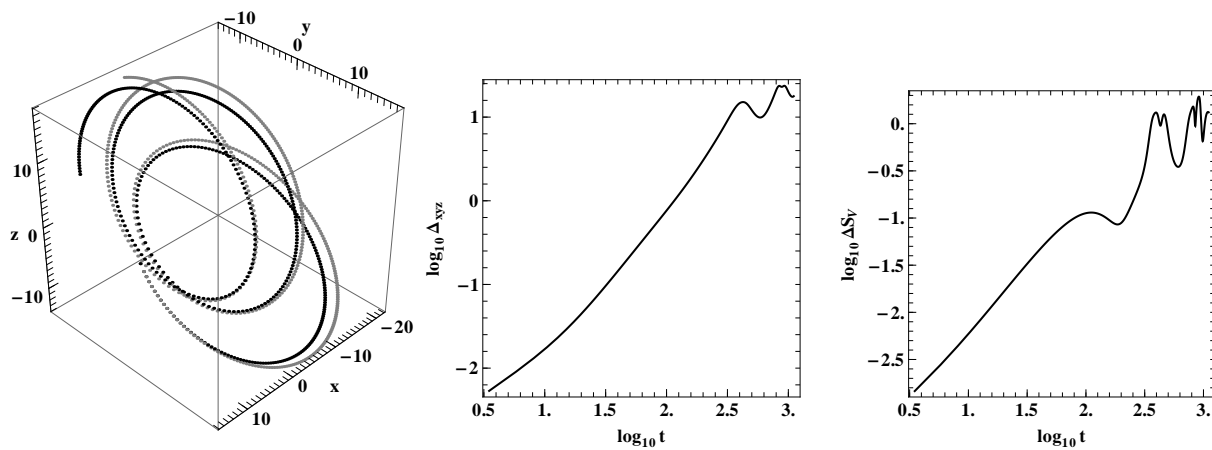


FIG. 5: The left panel shows how the orbit evolves through the MP equations (gray dots) and through the Hamilton's equations (black dots) in the configuration space x , y , z , when we use the initial conditions given in Fig. 1. The central panel shows the logarithm of the Euclidean distance in the configuration space between these two orbits as a function of the coordinate time. The right panel shows the logarithm of the Euclidean norm of the difference between the spin vectors of these two orbits as a function of the coordinate time.

5.3. Comparison for very small spin

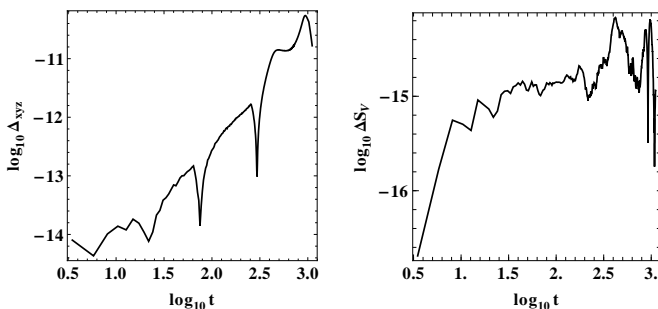


FIG. 6: The left panel shows the logarithm of the Euclidean distance in the configuration space between an orbit calculated with the MP equations and an orbit calculated with the Hamilton equations as a function of the coordinate time. For the orbits we have used the initial conditions given in Fig. 2. The right panel shows the logarithm of the Euclidean norm of the difference between the spin vectors of these two orbits as a function of the coordinate time.

By decreasing the measure of the particle's spin to the level of $S = 10^{-8}$, we get the initial setup given in Fig. 2. The Euclidean distance between the evolutions of the MP equations and the Hamilton equations (left panel of Fig. 6) drops to a level which is near the precession of our simulations. Therefore, practically, the two orbits should not discern. This seems to be the picture we get from the Euclidean norm of the difference between the spin vectors as well (right panel of Fig. 6). Moreover, it is also evident that the distance between the two orbits does not exceed the diameter of the disc of centers of mass defined by the Möller radius for the coordinate time we have computed. Therefore, it is reasonable to say that

the two orbits obtained by two different formalisms do correspond to the same particle and thus infer that the Hamiltonian is indeed valid for small spin values. However, this picture might be a little bit illusive. The order of the spin is $S = 10^{-8}$, and, thus, what we see in fact is that the relative difference, i.e., $\Delta S_v/S \approx 10^{-8}$ is of the order of the spins' magnitude. In other words, in the spin space the evolution of the two orbits does not agree completely. The reason that in the configuration space the orbits appear to be identical, while in the spin space the agreement is not at the same level, is that we are in the geodesic limit, and the evolution of the orbits is almost independent from the spins.

The bottom row of Fig. 7 supports the claim that when $S = 10^{-8}$, we are at the geodesic limit, and the evolution does not depend on the spins. In the left panel of the bottom row in Fig. 7, the relative errors of the Hamiltonian function,

$$\Delta H = \left| 1 - \frac{H(t)}{H(0)} \right|, \quad (69)$$

lie at the computation precession level for both the MP orbit (gray line) and the Hamiltonian orbit (black line), while the level of the relative error (66) in the measure of the spin vectors,

$$S^2 = S_I S^I, \quad (70)$$

is not as well preserved for the MP case (gray line) as for the Hamiltonian case (black line in the right panel of the bottom row in Fig. 7). Notice that, as stated above, in the case of the MP equation, we can get the value of the Hamiltonian function H and of the square of the spin measure S^2 by transforming the set of variables $\{x^\mu, p^\mu, S^{\mu\nu}\}$ into the set $\{x^i, P^i, S^I\}$ and substituting the transformed set into Eq. (35) and Eq. (70) respectively.

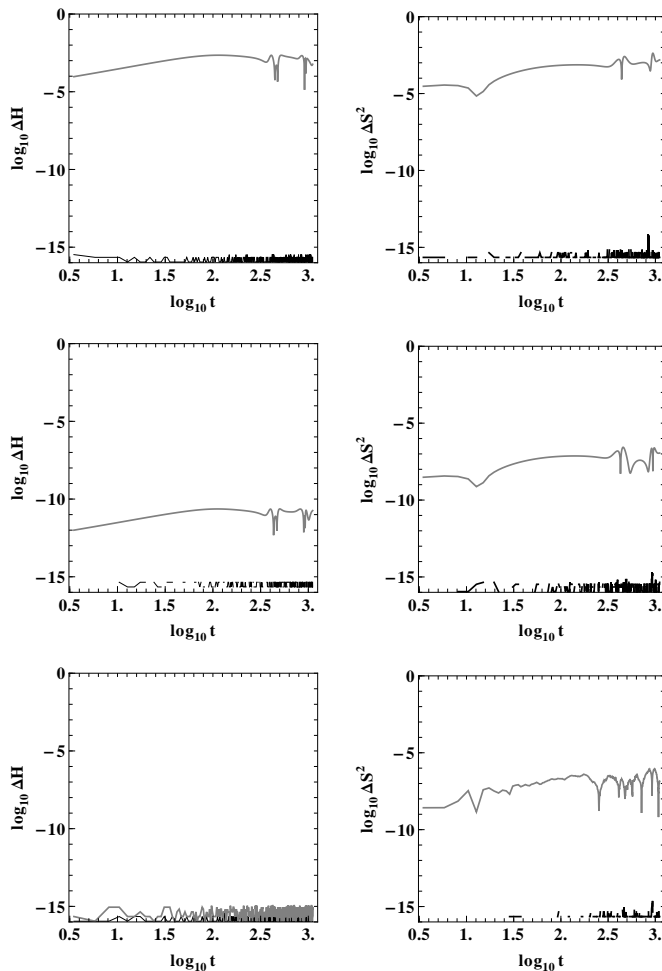


FIG. 7: The top row of panels corresponds to the orbits of Fig. 5, while the bottom row of panels corresponds to the orbits of Fig. 6. The middle row of panels corresponds to initial conditions similar to Fig. 1 only instead of spin measure $S = 1$ we set $S = 10^{-4}$. The gray lines represent the evolution of the MP equations, while the black lines represent the evolution of the Hamilton equations. The left column of panels shows the relative error in the preservation of the Hamiltonian function, while the right shows the preservation of the spin.

5.4. Behavior of the constants of motion and scaling with the spin

When we raise the measure of the particle spin to $S = 10^{-4}$, then the relative error of the MP spin (Eq. (70)) remains practically at the same level (gray line in the right panel of the middle row in Fig. 7) as in the $S = 10^{-8}$ case. This does not hold for the relative error of the Hamiltonian function (gray line in the left panel of the middle row in Fig. 7) which is not at the computation precession level anymore. This shows that the motion is no longer in the geodesic limit. However, both ΔS^2 and ΔH for the MP orbit lie at acceptable levels, which shows that for this magnitude of the particle spin, the

MP equations and the Hamilton equations seem to be in agreement.

This agreement breaks when $S = 1$. The top row of Fig. 7 shows that when $S = 1$, the relative errors, ΔH and ΔS^2 are at the same quite high level for the MP orbit. These relatively large values confirm the departure between the MP equations and the corresponding Hamiltonian that we see in Fig. 5.

The black lines for all panels of Fig. 7 are at the highest accuracy the computation accuracy allows, which means that apart from round-off error, the Gauss scheme we applied integrates accurately the system of the Hamilton equations, but also that the interpolation scheme we applied to match the coordinate times works quite well.

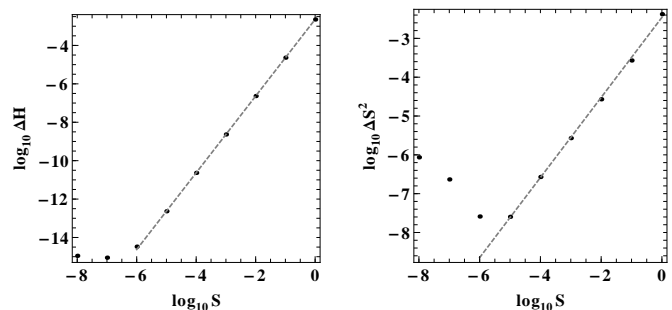


FIG. 8: The left panel shows the relative error of the Hamiltonian ΔH of orbits evolved through the MP equations for different spin measures S of the particle, while the right panel shows the corresponding preservations of the measure of the 3-vector ΔS^2 . The black dots correspond to the maximum values of ΔH , ΔS^2 , respectively, for each S . The dashed lines are linear fits of the form $\log_{10} \Delta H = a \log_{10} S + b$, and $\log_{10} \Delta S^2 = c \log_{10} S + d$, respectively, for data with $S > 10^{-6}$, where $a = 1.9968 \pm 0.0015$, $b = -2.644 \pm 0.004$, and $c = 1.031 \pm 0.015$, $d = -2.46 \pm 0.06$.

As at the end of the previous Section, we can investigate the scaling of the constants of motion with the spin in more detail by taking the maxima of their relative errors the MP equations, for different values of the measure of the particle's spin. The result is shown in Fig. 8. Again, as in Fig. 4, the precession of our computations and the scaling due to the spin measure shape the figure. We see a plateau at the left panel of Fig. 8 for ΔH due to the computational precession, while in the right panel of Fig. 8 we see that ΔS^2 increases, which is due to the smallness of the spin components. Even if we had applied a special integration scheme respecting these small quantities, this scheme could not follow below a threshold either. This threshold is in our case $S = 10^{-6}$. When the scaling with the spin dominates ($S > 10^{-6}$), the linear fits show that $\Delta H \propto S^2$, while $\Delta S^2 \propto S$. These proportionalities are expected as we explain next.

By construction the Hamiltonian function H of a spinning particle is accurate up to linear order of the particle spin. Hence, when compared with the value of the

Hamiltonian function yielded from the evolution of the MP equations $H_{MP}(t)$, the difference between the two Hamiltonian function values should differ by terms of the order $O(S^2)$, i.e.,

$$H_{MP}(t) \approx H(t) + O(S^2) . \quad (71)$$

However, since we have chosen the same initial conditions for both evolution schemes, it holds that $H_{MP}(0) = H(0)$. Thus, the relative error (69) for the MP equations reads

$$\begin{aligned} \Delta H &= \left| \frac{H_{MP}(t) - H_{MP}(0)}{H_{MP}(0)} \right| \\ &\approx \left| \frac{H(t) - H(0)}{H(0)} + \frac{O(S^2)}{H(0)} \right| . \end{aligned} \quad (72)$$

Since we do not expect the relative error $\frac{H(t)-H(0)}{H(0)}$ to depend on the value of the particle's spin, and this expectation is confirmed by the numerical findings (black lines in the left column of Fig. 7), we get the scaling $\Delta H \propto S^2$ of Fig. 8.

In order to explain the scaling of the relative error ΔS^2 , we use a similar way of reasoning. The preservation of the spin for the Hamiltonian formalism (70) is S^2 , thus a reasonable expectation is that for the MP case we should get values $S^2_{MP}(t)$ from Eq. (70) which differ from the Hamiltonian case at order $O(S^3)$, i.e.,

$$S^2_{MP}(t) \approx S^2(t) + O(S^3) . \quad (73)$$

Furthermore, we have $S^2_{MP}(0) = S^2(0)$. Thus, the relative error (66) for the MP equations reads

$$\begin{aligned} \Delta S^2 &= \left| \frac{S^2_{MP}(t) - S^2_{MP}(0)}{S^2_{MP}(0)} \right| \\ &\approx \left| \frac{S^2(t) - S^2(0)}{S^2(0)} + \frac{O(S^3)}{S^2(0)} \right| , \end{aligned} \quad (74)$$

which explains why we see that $\Delta S^2 \propto S$ in the right panel of Fig. 8.

If we take as a criterion the convergence of the constants of motion shown in Fig. 8, and consent that a relative error of the level of 10^{-6} is adequate to state that the different formalisms have converged, then from our comparison the Hamiltonian formalism is in agreement with the MP equations for the NW SSC when the measure of the particle's spin is $S < 10^{-4}$. When we reach $S \approx 10^{-6}$, the effect of the spin appears not to be important anymore, and the orbit evolves like a geodesic, i.e., it does not depend on the spin.

6. CONCLUSIONS

We have compared the evolutions of a spinning test particle in Kerr spacetime governed by different equations of motion. We first evolved the orbits prescribed by

the MP equations, once supplemented by the Tulczyjew SSC and once by the Newton-Wigner SSC. Our simulations indicate a linear in the spin scaling of the difference between the respective orbits. We also found that, in the case of the NW SSC, the four-momentum is conserved up to linear order in the square of the test particle's spin, i.e. $\Delta\mu^2 \propto S^2$. In a second series of experiments we compared orbits given by the MP equations plus NW SSC with orbits obtained via the Hamiltonian formalism of [7]. Here, too, the difference between the respective orbits, which is quite significant for large spins of the order of one, decreases linearly as a function of the square of the test particle's spin, i.e. $\Delta H \propto S^2$, which agrees with the analysis given in [7]. According to our analysis, the Hamiltonian formalism of the spinning particle appears to be relevant in the range $10^{-6} < S < 10^{-4}$. For values of the spin smaller than 10^{-6} we can ignore the part of the Hamiltonian describing the spin evolution and keep the non-spinning part, and for spin values greater than 10^{-4} , our numerical results show that the Hamiltonian formalism is not in good agreement with the MP equations. Anyhow, the aforementioned range, where the Hamiltonian formalism is relevant, is appropriate for astrophysical binary systems of extreme mass ratio. Moreover, as our simulations showed that the CPU effort for the Hamilton equations of motion is far smaller than the computational cost for the MP equations, we find appropriate the use of these equations for simulations of test particles with small spins. When, in addition, favorable numerical methods, such as the one presented in this work, are applied, reliable results can be obtained within a short period of time.

Acknowledgments

This work was supported by the DFG grant SFB/Transregio 7, by the DFG Research Training Group 1620 "Models of Gravity" and by the "Centre for Quantum Engineering and Space-Time Research (QUEST)". We specially would like to thank Oldrich Semerák for his useful suggestions and remarks.

Appendix A: Numerical integration of the MP equations

Seen from a numerical point of view, the initial value problem (56) reads

$$\frac{d\mathbf{y}}{d\tau} = f(\mathbf{y}) , \quad (A1)$$

$$\mathbf{y}(\tau = 0) = \mathbf{y}_0 . \quad (A2)$$

with $\mathbf{y} = (t, r, \dots, S^{\theta\phi}, S^{\theta\theta})^T \in \mathbb{R}^{24}$ and $f : \mathbb{R}^{24} \rightarrow \mathbb{R}^{24}$. If this system was of Hamiltonian canonical form, symplectic integration schemes would be the most natural

choice for their numerical solution. They almost exactly preserve a differential equation's constants of motion and, unless for standard integration schemes, their overall numerical error grows only slowly as a function of the total integration time even for larger step sizes. Therefore, simulations over long time spans can be carried out efficiently. Unfortunately, the MP equations are not of Hamiltonian canonical form. But, they can be interpreted as the Euler-Lagrange equations of a suitable Lagrangian action, see, e.g., [28–30]. What then saves the day is that the flow of symplectic integration schemes can be interpreted as the solution of the Euler-Lagrange equations of a discretization of the Lagrangian action. Schemes with this property are called *variational integrators* and they only rely on the existence of a Lagrangian structure for their favorable behavior. For example they are known to exactly preserve an equation of motion's first integrals which are quadratic in the phase space variables. This implies that a variational integration scheme applied to the MP equations with T SSC will conserve the four-momentum μ^2 and the spin length S^2 up to numerical round-off errors. An extensive discussion of this topic can be found in the monograph [19], chapter VI.6. One prominent example of variational integrators is Gauss Runge-Kutta methods which have been shown to be the most efficient and accurate integrators in many general relativistic applications, see, e.g., [20, 21]. Motivated by these results, we choose this kind of variational integrator for the solution of the MP equations. Here we briefly summarize some of their properties.

An s -stage Gauss Runge-Kutta scheme is a collocation method, i.e. an implicit Runge-Kutta scheme

$$\mathbf{y}_{n+1} = \mathbf{y}_n + h \sum_{i=1}^s b_i f(\mathbf{Y}_i) , \quad (\text{A3})$$

$$\mathbf{Y}_i = \mathbf{y}_n + h \sum_{j=1}^s a_{ij} f(\mathbf{Y}_j), \quad i = 1, \dots, s , \quad (\text{A4})$$

with coefficients

$$a_{ij} = \int_0^{c_i} l_j(t) dt , \quad (\text{A5})$$

$$b_j = \int_0^1 l_i(t) dt , \quad (\text{A6})$$

where the stages c_1, \dots, c_s are chosen as

$$c_i = \frac{1}{2}(1 + \tilde{c}_i) , \quad (\text{A7})$$

with \tilde{c}_i being the roots of the Legendre-polynomial of degree s . Here, h denotes the time step size, Y_i , $i = 1, \dots, s$, are the so-called inner stage values and \mathbf{y}_n denotes the numerical approximation to the solution \mathbf{y} at time $\tau = nh$. The functions $l_i(t)$ are the Lagrange-polynomials of degree s ,

$$l_i(t) = \prod_{i \neq j} \frac{t - c_j}{c_i - c_j} . \quad (\text{A8})$$

Gauss Runge-Kutta methods have a convergence order $\mathcal{O}(h^{2s})$ which is the highest possible order among collocation schemes, e.g., [32]. When integrating a time step with a Gauss Runge-Kutta scheme, one first solves the system of implicit equations (A4) via a fixed-point iteration

$$\mathbf{Y}_i^{k+1} = \mathbf{y}_n + h \sum_{j=1}^s a_{ij} f(\mathbf{Y}_j^k) . \quad (\text{A9})$$

This, of course, requires more calculations per time step than an explicit scheme with the same number of stages. But, this extra effort is more than offset by the high accuracy of Gauss collocation methods which allows us to apply them with a much larger step size. Detailed information on their implementation is given in [21], Sec. 7, and [19], chapters VIII.5 and VIII.6.

To illustrate the favorable behavior of Gauss collocation methods, we compare the performance of a 4-stage scheme with step size $h = 1$ and a standard 5-th order explicit Cash-Karp scheme as proposed in [33] with a step size $h = 0.1$, when applied to the MP equations with T SSC and initial data given by $E = 0.95$, $J_z = 3.0$, $S = 1$, $M = 1$, $\mu = 1$, $a = 0.9$, $r = 6.7$, $\theta = \frac{\pi}{2} + 0.1$, $p_r = 0.1$, $S_r = 0.1$, $S_\theta = 0.01$. In Fig. 9, we plot for both integrators the relative error in the energy,

$$\Delta E(\tau) = \frac{|E(\tau) - E(0)|}{|E(0)|} , \quad (\text{A10})$$

and the corresponding relative error in the z angular momentum as a function of integration time τ . We observe that the Gauss Runge-Kutta method, which is also faster, gives much more precise results.

An additional obstacle for simulations in the NW SSC case is that the tangential velocity v^μ is only given implicitly by Eq. (27). (N.b.: Apart from the apparent v^ν in the first term on the right hand side, the covariant derivative of ω_ν implies a linear dependence on v^ν in the second term on the rhs as well, i.e., $\frac{D \omega_\nu}{d\tau} = \dot{\omega}_\nu - \Gamma_{\nu\mu}^\kappa \omega_\kappa v^\mu$.) Setting $\vec{v} := (v^t, v^r, v^\phi, v^\theta)^T \in \mathbb{R}^4$, the implicit equation for v^μ is qualitatively given by

$$\vec{v} = A(x^\mu, p^\mu, S^{\mu\nu}) \vec{v} \quad (\text{A11})$$

for a certain matrix $A \in \mathbb{R}^{4 \times 4}$. Theoretically there are two possibilities to cope with the implicitness in the velocities which we will describe now.

- Denoting the first four components of Y_i and $f(Y_i)$ by Y_i^x and $f^x(Y_i)$, and the other components by Y_i^p , Y_i^S , $f^p(Y_i)$, and $f^S(Y_i)$ we can augment the system of implicit equations (A4) by adding the implicitly given quantity \vec{v}_i which denotes the tangential velocity v^μ at the inner stage Y_i . This yields

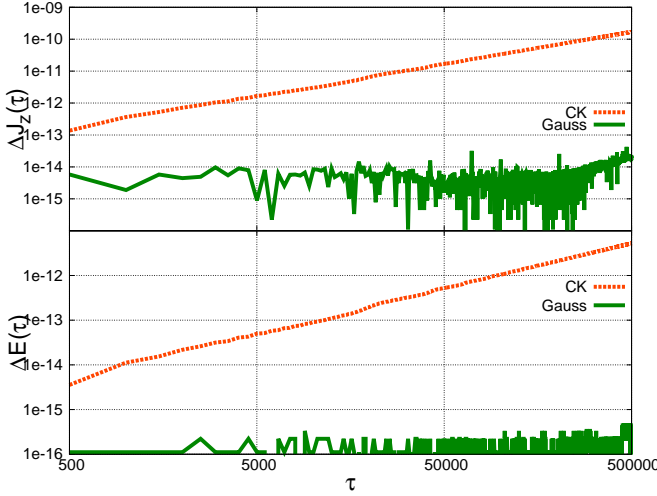


FIG. 9: The relative error of the z angular momentum, ΔJ_z , (top panel) and the relative error of the energy, ΔE , (bottom panel) against integration time τ for the 4-stage Gauss scheme with step size $h = 1$ and the 5-th order Cash-Karp scheme with step size $h = 0.1$ applied to the initial value problem (56) with initial data as stated in the text. CPU-time was 214.1s for the Gauss Runge-Kutta scheme and 422.7s for the Cash-Karp scheme.

the system

$$\begin{pmatrix} \vec{v}_i \\ \mathbf{Y}_i^x \\ \mathbf{Y}_i^p \\ \mathbf{Y}_i^S \end{pmatrix} = \begin{pmatrix} A(\mathbf{Y}_i^x, \mathbf{Y}_i^p, \mathbf{Y}_i^S) \vec{v}_i \\ \mathbf{y}_n^x + h \sum_{j=1}^s a_{ij} \vec{v}_i \\ \mathbf{y}_n^p + h \sum_{j=1}^s a_{ij} f^p(\mathbf{Y}_i^x, \mathbf{Y}_i^p, \mathbf{Y}_i^S, \vec{v}_i) \\ \mathbf{y}_n^S + h \sum_{j=1}^s a_{ij} f^S(\mathbf{Y}_i^x, \mathbf{Y}_i^p, \mathbf{Y}_i^S, \vec{v}_i) \end{pmatrix}, \quad (A12)$$

$i = 1, \dots, s$,

to which, again, a fixed-point iteration can be applied. However, for this iteration to converge, it needs to satisfy

$$\left\| \begin{pmatrix} \vec{v}_i^{k+2} \\ \mathbf{Y}_i^{k+2} \end{pmatrix} - \begin{pmatrix} \vec{v}_i^{k+1} \\ \mathbf{Y}_i^{k+1} \end{pmatrix} \right\| \leq \left\| \begin{pmatrix} \vec{v}_i^{k+1} \\ \mathbf{Y}_i^{k+1} \end{pmatrix} - \begin{pmatrix} \vec{v}_i^k \\ \mathbf{Y}_i^k \end{pmatrix} \right\| , \quad (A13)$$

which cannot be guaranteed when $A(\mathbf{Y}_i^x, \mathbf{Y}_i^p, \mathbf{Y}_i^S)$ is of large norm. Numerical tests have shown that there are indeed problems with the convergence. Hence, for all its conceptual beauty, the approach of an augmented implicit system is of no practical use.

- With I denoting the 4×4 identity matrix, we can rewrite the implicit equation for the velocities (A11) as

$$0 = (I - A) \vec{v} =: B \vec{v} . \quad (A14)$$

Thus, from an algebraical point of view, the vector consisting of the components of the 4-velocity is an element of the nullspace $\text{Ker}(B)$ of the matrix B

which here is a one-dimensional subspace. Consequently, we can determine the tangential velocity at an internal stage by the following procedure

1. Calculate $B(\mathbf{Y}_i^x, \mathbf{Y}_i^p, \mathbf{Y}_i^S) = I - A(\mathbf{Y}_i^x, \mathbf{Y}_i^p, \mathbf{Y}_i^S)$.
2. Calculate the singular-value-decomposition of B , i.e.,

$$B = U \Sigma V^T , \quad (A15)$$

with $\Sigma = \text{diag}(\sigma_1, \sigma_2, \sigma_3, \sigma_4)$ and $U^T U = V^T V = \delta_{ij}$, $i, j = 1, \dots, 4$ (For more information on the singular value decomposition, see, e.g., [33], chapter 2.6). The nullspace of B is then spanned by the column of the orthonormal matrix $V_{\cdot, i}$ that corresponds to the only singular value σ_i which is equal to 0.

3. The tangential velocity is now obtained by renormalizing $V_{\cdot, i}$ in order to have $v^\mu v_\mu = -1$.

This procedure is very robust and the computational cost for the calculation of the matrix B and the singular value decomposition is far less than the computational cost for the calculation of the other quantities which are needed anyway. This could be confirmed experimentally when comparing CPU times for simulations with T SSC and NW SSC for similar initial values. For all the simulations done in the preparation for this work, the CPU times in the NW SSC case were only slightly higher than those for the T SSC case where the velocities could be determined explicitly via Eq. (24).

Last, we turn to the numerical integration of the Hamiltonian formalism in the next section.

Appendix B: Numerical integration of the Hamiltonian equations

The Hamiltonian equations considered in this study have a so-called *Poisson structure*, that is, with $\mathbf{y} = (P_r, P_\theta, P_\phi, r, \theta, \phi, S_1, S_2, S_3)^T \in \mathbb{R}^9$, they can be written as

$$\dot{\mathbf{y}} = B(\mathbf{y}) \nabla H(\mathbf{y}) , \quad (B1)$$

where $B : \mathbb{R}^9 \rightarrow \mathbb{R}^{9 \times 9}$ is a skew-symmetric matrix-valued function. In our case, this function $B(\mathbf{y})$ is given by

$$B(\mathbf{y}) = \begin{pmatrix} 0 & -I_{3 \times 3} & 0 \\ I_{3 \times 3} & 0 & 0 \\ 0 & 0 & B_1(\mathbf{y}) \end{pmatrix} , \quad (B2)$$

with

$$I_{3 \times 3} = \begin{pmatrix} 1 & 0 & 0 \\ 0 & 1 & 0 \\ 0 & 0 & 1 \end{pmatrix}, \quad (\text{B3})$$

$$B_1(\mathbf{y}) = \begin{pmatrix} 0 & -S_3 & S_2 \\ S_3 & 0 & -S_1 \\ -S_2 & S_1 & 0 \end{pmatrix}. \quad (\text{B4})$$

For such $B(\mathbf{y})$, there exists a smooth transformation to new coordinates \mathbf{z} , for which the equations of motion are of symplectic form

$$\dot{\mathbf{z}} = J^{-1} \nabla H(\mathbf{z}), \quad (\text{B5})$$

$$J = \begin{pmatrix} 0 & I_{4 \times 4} \\ -I_{4 \times 4} & 0 \end{pmatrix}, \quad (\text{B6})$$

see [21, 34]. The idea how to find this transformation is based on the conservation of the spin length $S = \sqrt{S_1^2 + S_2^2 + S_3^2}$ by the eqs. (B1). Thus, the three dimensional spin $\mathbf{S} = (S_1, S_2, S_3)^T$ can be given as a function of two variables α and ξ via

$$\mathbf{S} = S \begin{pmatrix} \sqrt{1 - \xi^2} \cos(\alpha) \\ \sqrt{1 - \xi^2} \sin(\alpha) \\ \xi \end{pmatrix}. \quad (\text{B7})$$

One can then show that

$$\dot{\xi} = -\frac{\partial H}{\partial \alpha}, \quad (\text{B8})$$

$$\dot{\alpha} = \frac{\partial H}{\partial \xi} \quad (\text{B9})$$

hold, see, e.g. [21]. Hence, for the variables $\mathbf{z} = (P_r, P_\theta, P_\phi, \xi, r, \theta, \phi, \alpha)$, the equations of motion indeed take the form (B5). Whenever a system can be smoothly transformed to symplectic form, it can be evolved by symplectic integration schemes. Therefore, for our studies of the Hamiltonian formalism of [7], we follow [21] and use Gauss Runge-Kutta schemes which have already been presented in the last section [36]. In order to show their favorable behavior, we evolve the Hamiltonian system for initial data $M = 1, m = 1, a = \frac{1}{10}, r = 15, \theta = \frac{\pi}{2}, \phi = 0, P_r = 0, P_\theta = 3.69336, P_\phi = J_z = 3.8, S_1 = \frac{1}{\sqrt{2}}, S_2 = \frac{1}{\sqrt{3}}, S_3 = \frac{1}{\sqrt{6}}$ and plot, in Fig. 10, the relative error of the Hamiltonian (69) once for the Gauss Runge-Kutta method with $s = 4$ inner stages and once for the 5th order explicit Cash-Karp scheme. For the explicit method we observe a linear growth in the error while there is no significant error during the whole simulation for the Gauss scheme. This is in spite of the latter's much smaller CPU time. With regard to the computational effort, we also notice that it is much smaller than in the case of the full MP equations, although both cases were tested on

the same machine. This gives another practical reason to consider the Hamiltonian approximation.

In our comparison of the orbits given by the MP equations with those of the Hamiltonian formalism, the concerning simulations have to produce output for the same

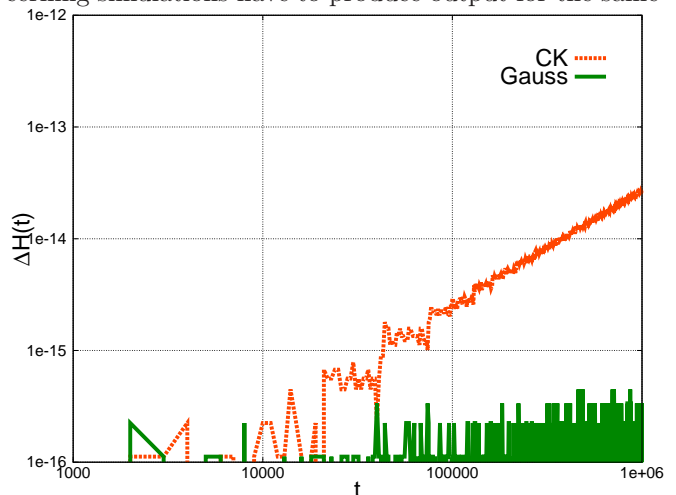


FIG. 10: The relative error of the Hamiltonian, ΔH against integration time t for the 4-stage Gauss scheme with step size $h = 2$ and the 5-th order Cash-Karp scheme with step size $h = 0.2$ applied to the initial value problem (B1) with initial data as stated in the text. CPU-time was 7.83s for the Gauss Runge-Kutta scheme and 24, 7s for the Cash-Karp scheme.

coordinate times. To avoid having to reformulate the MP equations for the coordinate time as evolution parameter, we proceed as follows. In the simulation of the MP equations, output is produced at uniform distances in the evolution parameter proper time. The output also comprises the corresponding coordinate times. These are then fed as input to the Hamiltonian simulations -for example under the name $t_{\text{output required}}$. Now, if in the simulation with uniform steps in the evolution parameter coordinate time t , between times t_i and t_{i+1} say, one passes one of the prescribed times for which output is required, $t_{\text{output required}}$, one can take use of the interpolation property of the collocation schemes to comfortably obtain output at no computational extra cost. It is well known that the interpolation polynomial $\mathbf{u}(t)$ through the points $(0, \mathbf{y}_n), (c_i, \mathbf{Y}_i), i = 1, \dots, s$, stays $\mathcal{O}(h^s)$ close to the exact solution of the equation of motion, and, hence, also to the numerical calculated trajectory, see, e.g., [32]. We thus only have to evaluate $\mathbf{u}(t)$ at time $t_{\text{output required}} - t_i$ which yields an approximation of the solution at time $t_{\text{output required}}$ which is exact up to an error of $\mathcal{O}(h^s)$. The interpolation polynomial itself can be calculated very quickly with the so-called Horner scheme

$$\begin{aligned}
\mathbf{u}(t) &= \mathbf{y}_i + (t - 0) (\delta^1[0, hc_1] + (t - hc_1) (\delta^2[0, hc_1, hc_2] + (t - hc_2) (\dots (t - hc_{s-1}) \delta^s[0, hc_1, \dots, hc_s] \dots)) \ , \\
\delta^1[0, hc_1] &= \frac{\mathbf{Y}_1 - \mathbf{y}_i}{hc_1 - 0} \ , \\
\delta^k[0, hc_1, \dots, hc_k] &= \frac{\delta^{k-1}[hc_1, \dots, hc_k] - \delta^{k-1}[0, hc_1, \dots, hc_{k-1}]}{hc_k - 0} \ .
\end{aligned} \tag{B10}$$

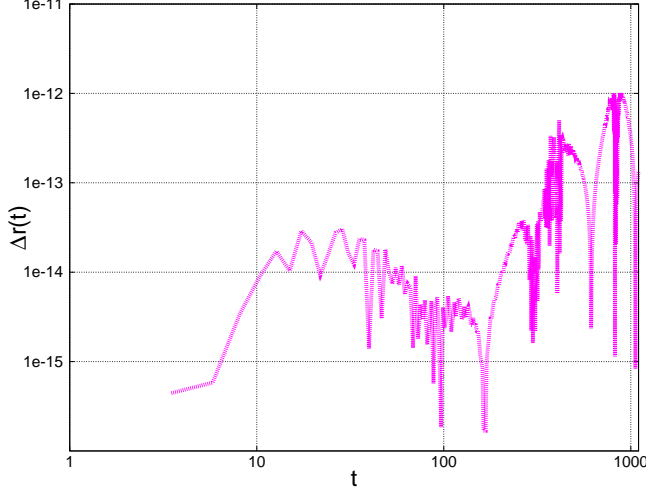


FIG. 11: The relative difference, Δr , between the radial distance calculated with the interpolation method and the radial distance calculated via the cumbersome method with extra integration steps plotted against output time t .

The more intricate way of producing output at the desired times would be the following:

- When having passed an output time t_{output} required between t_i and t_{i+1} , go back to t_i .
- Change $h \rightarrow h_{\text{new}} = t_{\text{output}} - t_i$.
- Evolve the system until $t = t_{\text{output}}$ required with step size h_{new} and produce output.
- Go back to t_i and go on integrating with step size h . (Note that this is necessary as the scheme would lose its symplectic structure when applied with different step sizes, see, e.g. [19], chapter VIII.)

In order to illustrate that this cumbersome procedure is not worth the additional effort, we again consider the data which yielded Fig. 5 and, for every coordinate time t , for which Δ_{xyz} was plotted in the central panel of that figure, we plot the relative difference in the radial distance at those times between the interpolation method and the cumbersome method,

$$\Delta r(t) = \frac{|r_{\text{interpolation}}(t) - r_{\text{cumbersome}}(t)|}{r} \ . \tag{B11}$$

In Fig. 11, we can observe that the difference is negligible.

-
- [1] M. Mathisson, *Acta Phys. Polonica* **6**, 163 (1937)
- [2] A. Papapetrou, *Proc. R. Soc. London Ser. A* **209**, 248 (1951)
- [3] O. Semerák, *Mon. Not. R. Astron. S.* **308**, 863 (1999)
- [4] K. Kyrián, and O. Semerák, *Mon. Not. R. Astron. S.* **382**, 1922 (2007)
- [5] W. Tulczyjew, *Acta Phys. Polonica* **18**, 393 (1959)
- [6] T. D. Newton and E. P. Wigner, *Rev. Mod. Phys.* **21**, 400 (1949)
- [7] E. Barausse, E. Racine, and A. Buonanno, *Phys. Rev. D* **80**, 104025 (2009)
- [8] E. Barausse, and A. Buonanno, *Phys. Rev. D* **81**, 084024 (2010)
- [9] T. Hinderer, A. Buonanno, A. .H. Mroué, D. A. Hemberger, G. Lovelace, H. P. Pfeiffer, L. E. Kidder, M. A. Scheel, B. Szilagy, N. W. Taylor, S. A. Teukolsky, *Phys. Rev. D* **88**, 084005 (2013)
- [10] W. G. Dixon, *Proc. R. Soc. London Ser. A* **314**, 499 (1970); *Proc. R. Soc. London Ser. A* **319**, 509 (1970);
- [11] Y. Mino, M. Shibata, and T. Tanaka, *Phys. Rev. D* **53**, 622 (1996); T. Tanaka, Y. Mino, M. Sasaki, and M. Shibata, *Phys. Rev. D* **54**, 3762 (1996)
- [12] J. Steinhoff, and D. Puetzfeld, *Phys. Rev. D* **86**, 044033 (2012)
- [13] M. D. Hartl, *Phys. Rev. D* **67**, 024005 (2003); *Phys. Rev. D* **67**, 104023 (2003)
- [14] D. Bini, and A. Geralico, *Phys. Rev. D* **89**, 044013 (2014)
- [15] W. G. Ramírez, A. A. Deriglazov, and A. M. Pupasov-Maksimov, *J. High Energy Phys.* **3**, 109 (2014)
- [16] E. Hackmann, C. Lämmerzahl, Y. N. Obukhov, D. Puetzfeld, and I. Schaffer, arXiv:1408.1773
- [17] J. Steinhoff, G. Schäfer, and S. Hergt, *Phys. Rev. D* **77**, 104018 (2008)
- [18] J. Steinhoff, *Annal. Phys* **523**, 296 (2011)
- [19] E. Hairer, C. Lubich and G. Wanner, *Geometric numerical integration. Structure-preserving algorithms for ordinary differential equations* (Springer, 2006), 2nd ed.
- [20] J. Seyrich and G. Lukes-Gerakopoulos, *Phys. Rev. D* **86**, 124013 (2012)
- [21] J. Seyrich, *Phys. Rev. D* **87**, 084064 (2013)
- [22] S. Y. Zhong, X. Wu, S.-Q. Liu and X.-F. Deng, *Phys. Rev. D* **82**, 124040 (2010)

- [23] L. Mei, M. Ju, X. Wu and S.-Q. Liu, *Mon. Not. R. Astron. S.* **435**, 2246 (2013)
- [24] F. A. E. Pirani, *Acta Phys. Polonica* **15**, 389 (1956)
- [25] L. F. Costa, C. Herdeiro, J. Natário and M. Zilhão, *Phys. Rev. D* **85**, 024001 (2012)
- [26] S. Suzuki, and K.-I. Maeda, *Phys. Rev. D* **55**, 4848 (1997)
- [27] C. Möller, *Ann. Inst. Henri Poincaré* **11**, 251 (1949)
- [28] K. Westpfahl, *Annalen Phys.* **477**, 361 (1969)
- [29] I. Bailey, and W. Israel, *Commun. Math. Phys.* **42**, 65 (1975)
- [30] R. A. Porto, *Phys. Rev. D* **73**, 104031 (2006)
- [31] X. Wu, T.-Y. Huang, and H. Zhang, *Phys. Rev. D* **74**, 083001 (2006); P. Suková, and O. Semerák, *Mon. Not. R. Astron. S.* **436**, 978 (2013); G. Lukes-Gerakopoulos, *Phys. Rev. D* **89**, 043002 (2014)
- [32] E. Hairer, S. P. Nørsett and G. Wanner, *Solving Ordinary Differential Equations I* (Springer, 1993), 2nd ed.
- [33] W. Press, S. Teukolsky, W. Vetterling and B. Flannery, *Numerical Recipes in C. The art of scientific computing* (Cambridge University Press, 1992), 2nd ed.
- [34] X. Wu and Y. Xie, *Phys. Rev. D* **81**, 084045 (2010)
- [35] There is also another Hamiltonian formulation for the spinning particle [15] in which a noncommutative position coordinate is used instead of the canonical one.
- [36] As opposed to the approach in [21] we did not bother to rewrite the system in the variables z , because in the present case the additional cost of the one extra variable is negligible in comparison to the other computational effort.